Carbon Black Engineered Cementitious Composites - Mechanical and Electrical Characterization

Mo Li, Vincent W. J. Lin, Jerome P. Lynch and Victor C. Li

Synopsis: The protection and health monitoring of deteriorating concrete infrastructure requires a new generation of self-sensing structural materials that possess intrinsic damage tolerance but offer self-sensing capabilities that are tailored to diagnose states of cracking. Engineered Cementitious Composites (ECC) doped with carbon black (CB) nano-particles are proposed as highly damage-tolerant materials whose electrical properties can be correlated to strain and cracking. This study investigated the effect of CB dosage on the CB-ECC rheological, mechanical and electrical properties. By incorporating CB nano-particles into the ECC system while simultaneously controlling the rheological properties of the fresh mix, the fully cured CB-ECC elements achieved close-to-uniform PVA fiber and carbon black dispersion, reduced bulk resistivity by an order of magnitude, strain hardening behavior with tensile strain capacity of 0.26 to 1.38%, and reduced crack widths of 30 to 40 μm during tensile loading. Furthermore, all of the CB-ECC specimens exhibited prominent piezoresistive behavior with resistivity increasing in tandem with applied tensile strain, thereby indicating the potential of CB-ECC for strain and damage sensing.

Keywords: damage detection, electrical impedance, engineered cementitious composite, structural health monitoring

Mo Li: Dr. Li is an Assistant Professor in the Department of Civil and Environmental Engineering at the University of Houston. Her research interests are in advanced material technologies and high performance structural systems. Dr. Li received her Ph.D. (2009) and M.S. (2004) in Civil and Environmental Engineering from the University of Michigan. Prior to joining the University of Michigan, Dr. Li received her B.S.E (2001) in Civil and Environmental Engineering from Tongji University, China.

Vincent Lin: Mr. Lin is a Ph.D. Candidate in the Department of Civil and Environmental Engineering at the University of Michigan. His Ph.D. thesis explores of the use of the electrical properties of cementitious materials for strain sensing and damage detection. Prior to joining the University of Michigan, Mr. Lin received his M.E. (2008) and B.E. (2007) in Civil Engineering from the National University of Singapore.

Jerome P. Lynch: Dr. Lynch is an Associate Professor in the Department of Civil and Environmental Engineering at the University of Michigan. His research interests are in damage detection, structural health monitoring and advanced sensor technologies. Dr. Lynch received his Ph.D. (2002) and M.S. (1998) in Civil and Environmental Engineering from Stanford University. In 1997, Dr. Lynch received his B.E. in Civil and Environmental Engineering from The Cooper Union in New York City.

Victor C. Li: Dr. Li is E.B. Wylie Collegiate Chair Professor of Civil and Environmental Engineering at the University of Michigan. Dr. Li's expertise is in the development of sustainable cementitious materials for civil infrastructure systems based on micromechanics theory. Dr. Li received his Ph.D. (1981) in Solid and Structural Mechanics and his M.S. (1978) and B.S. (1977) in Mechanical Engineering and B.A. (1997) in Economics from Brown University. He is a fellow of ACI.

INTRODUCTION

Infrastructure systems are vital societal assets that support the operation of urban communities and provide the fundamental services necessary for the prosperous operation of a regional economy. Structural deterioration is a serious issue that affects all infrastructure systems. For concrete structural components, the general lack of material durability can lead to cracking, spalling and reinforcement corrosion. Similarly, for metallic structural components, corrosion and fatigue are issues of concern. If left uncheck, minor deterioration can lead to more serious damage states that require major and expensive rehabilitation of the structure. In some cases, undetected deterioration can lead to catastrophic failure of the structure (Wardhana and Hadipriono 2003). While visual inspection of infrastructure systems can identify structural problems, such methods are subjective and require labor-intensive investigation of the structure. To overcome the limitation of visual inspections, structural health monitoring (SHM) has emerged as a viable alternative. SHM entails the installation of sensors in the structure to measure its environment and behavior under loading. Sensor measurements are then used to identify signs of structural deterioration and damage.

There exist two major challenges associated with structural deterioration (*i.e.*, cracking) in concrete: (1) inadequate material performance, and (2) the limitations of current structural health monitoring (SHM) approaches to reliably detect it. Due to its inherent brittleness, concrete is susceptible to cracking and fracture failure modes. Cracking and fracture also lead to other common deterioration mechanisms such as the corrosion of embedded steel reinforcement and subsequent concrete cover spalling. For example, transverse cracking in bridge decks is one of the dominant deterioration processes for bridges in many regions of the United States (Saadeghvaziri and Hadidi 2005). Cracks accelerate the penetration of chloride ions and other corrosive agents into the concrete cover, leading to the initiation of reinforcement corrosion. These undesirable processes can be especially aggressive in marine environments or regions where deicing salts are applied in the winter. Cracking and corrosion reduce structural service lives and increase maintenance and repair requirements during the complete life cycle of the structure. For example, the U.S. spends about $8.3 billion annually to directly address corrosion in highway bridges (Rolander *et al.* 2001). Furthermore, indirect costs related to traffic delays and productivity losses often exceed by more than 10 times the direct cost of maintenance/repair/rehabilitation.

Early detection of deterioration in concrete structures is critical to minimizing the cost of managing and maintaining the structure. Within the SHM field, a number of technological advances have occurred that today allow sensors to be installed in an infrastructure system at low-cost. While general advances have been made, SHM technologies specifically customized for damage detection in concrete are still direly needed. This research study aims to address these limitations through the realization of multifunctional cementitious materials with intrinsic damage tolerance and endowed with self-sensing capability. Engineered Cementitious Composites (Li 2002; Li 2007), or ECC, provides great potential for developing such multifunctional materials for infrastructure systems. While containing similar ingredients as concrete or normal fiber reinforced concretes (FRC), ECC's microstructure is specially tailored through the use of micromechanical models to achieve strain-hardening behavior and ductility levels approximately 200 to 600 times that of concrete under tension (Fig. 1) (Li 1998; Li *et al.* 2002), thereby leading to high damage tolerances (Maalej *et al.* 1995). During strain-hardening, inelastic deformation is accompanied by microcracking with crack widths less than 100 μm (3.9×10^{-3} in.). ECC has a compressive strength the same order of magnitude as high strength concrete, but with an approximately 50% increase in compressive strain capacity. In this study, it is the electrical properties of ECC that are of great interest with ECC material strategically re-engineered to develop self-sensing characteristics. With structures already constructed worldwide using ECC materials (*e.g.,* as link beams in high-rise concrete buildings and deck surfaces in bridge structures), developing the material to act as a sensor would have tremendous benefit for identifying the deterioration and damage introduced in ECC components during normal operation and immediately following extreme events (e.g., earthquakes).

Resistivity of cementitious materials has been explored as a sensing functionality for hydration monitoring, composition assessment, and currently as an emerging method for measuring the material's mechanical state (Chen and Chung 1993; Peled *et al.* 2001; Ou and Han 2009). Cementitious materials are semiconductors with bulk resistivity ranging between 10^3 to 10^8 Ω-cm. Under an applied steady electric field, the ions in pore water are mobilized to create an electrical current. Piezoresistivity is defined as the percent change in material resistivity per unit strain. One benefit of self-sensing cementitious materials is that a measurement can be made wherever the material is; this opens a range of possibilities for distributed sensing with spatial mappings of conductivity (conductivity is the inverse of resistivity) correlated to strain and damage states. Toward this end, a variety of electrical impedance tomographic (EIT) sensing techniques have been recently proposed for cementitious materials including ECC (Hou and Lynch 2009).

While previous work in the field focused on the establishment of the piezoresistive behavior of FRC materials using conductive fibers, this study seeks to achieve a strain-hardening, self-sensing cementitious composite with crack widths controlled using polymeric fibers (*i.e.*, ECC). Specifically, the study seeks to modify the material properties of ECC through the inclusion of nanometer-scale carbon black to enhance bulk resistivity without affecting the rheological and mechanical properties of the composite. The benefits of the self-sensing multifunctional carbon-black ECC (CB-ECC) is two-fold. First, CB-ECC can serve as a durable material platform for future civil infrastructure defined by enhanced resistance to deterioration and damage (*e.g.* cracking, corrosion, cover spalling). Second, CB-ECC can provide the capability of distributed and direct sensing of damage by correlating measured material electrical properties to mechanical and physical behavior (*e.g.,* strain, cracking).

MATERIALS AND PROCESSING

The CB-ECC composite material is designed by selecting appropriate ingredients, controlling rheology during processing, and tailoring the composite design at the micrometer-scale. More specifically, the distribution of particle sizes and the combined amount of water and superplasticizer are determined to achieve a homogeneous cementitious composite material with a plastic viscosity that favors uniform dispersion of polyvinyl alcohol (PVA) fibers and nanometer-scale carbon black (CB) particles. Furthermore, to ensure tensile strain-hardening behavior of CB-ECC specimens in the hardened state, the synergistic interaction between the fibers, cementitious matrix (which contains dispersions of CB), and fiber-matrix interface is tailored based on micromechanics theory (Li 1993; Kanda and Li 1999) to achieve a composite that sequentially forms dense fields of microcracks under tension. The fundamental requirement for the formation of dense fields of microcracks under tension is that steady-state flat crack propagation prevails under tension (Marshall 1988; Li and Leung 1992). To ensure steady-state cracking, the crack tip toughness, $J_{tip,}$ must be less than the complementary energy, J_b', calculated from the fiber bridging stress, σ, versus crack opening, δ, relation, as shown in Equations 1 and 2:

$$J_{tip} \le \sigma_0 \delta_0 - \int_0^{\delta_0} \sigma(\delta) d\delta \equiv J_b' \quad (1)$$

$$J_{tip} = \frac{K_m}{E_m} \quad (2)$$

Here, σ_0 is the maximum bridging stress corresponding to the opening δ_0, K_m is the matrix fracture toughness, and E_m is the matrix Young's modulus. This energy-based criterion determines whether the crack propagation mode is steady-state flat cracking or Griffith cracking (Griffith 1921).

Apart from the energy criterion, another condition for pseudo-strain hardening is that the matrix tensile cracking strength, σ_c, must not exceed the maximum fiber bridging strength, σ_0,

$$\sigma_c < \sigma_0 \quad (3)$$

where σ_c is determined by K_m and pre-existing internal flaw sizes, a_0. While the energy criterion (*i.e.*, Equation 1) governs the crack propagation mode, the strength-based criterion (*i.e.*, Equation 3) controls the initiation of cracks. Satisfaction of both equations is necessary to achieve ECC strain-hardening behavior; otherwise, the composite behaves as a normal fiber reinforced concrete (FRC) with tension softening behavior (as shown in Figure 1).

The introduction of CB into the ECC matrix may have a fundamental impact on the performance of the resulting CB-ECC composite. The mixture proportions of three CB-ECC designs adopted in this study are summarized in Table 1. The dry ingredients used in the material design consist of Type I Portland cement (C), fine silica sand (S) with average and maximum grain sizes of 110 μm (0.004 in.) and 200 μm (0.008 in.), respectively, normal Class-F fly ash (FA), REC-15 polyvinyl alcohol (PVA) fibers, and carbon black nano-particles (CB). The fine size of the silica sand and large volume of fly ash reduce the crack tip energy, J_{tip} (compared to larger size river sand or coarse aggregates), in favor of the energy-based criterion (Equation 1). The spherical size of the fly ash particles also provides a "ball bearing" effect rendering the composite material more flowable in its fresh state. Furthermore, the spherical shape of the fly ash particle reduces the chemical bond while increasing the frictional bond of the fiber-matrix interface. The PVA fiber is 12 mm (0.47 in.) long, 39 μm (1.5×10^{-3} in) in diameter, and surface-coated with 1.2% by weight of a proprietary hydrophobic agent. The geometry and interfacial bonding properties of the fiber are specially tailored to achieve a high complementary energy, J_b', and high bridging strength, σ_0.

Introducing CB into the ECC system can enhance the composite's electrical properties, but will also have impacts on its mechanical behavior (*e.g.*, positively or negatively). In this study, CB with an average particle size of 30 nm (1.18×10^{-6} in.) and bulk resistivity of approximately 10^{-1} Ω-cm was incorporated at increasing ratios of weight to total cementitious ingredients (cement plus fly ash): 0.25%, 0.5% and 1% *wt*. While its weight percentage is small, the large surface area of the incorporated CB is relatively high because of the nanometer-scale particle size. This leads to a significant increase in plastic viscosity and a decrease in flowability. Further, the CB alters the hydration process and results in changes in the matrix microstructure and micro-parameters of CB-ECC such as σ_c and J_{tip}. Finally, the incorporation of CB into the ECC matrix can also affect the dispersion of the PVA fibers in addition to modification of the fiber-matrix interfacial properties, both of which impact J_b' and σ_0.

A mixture of the dry ingredients, including CB, was first prepared in a Hobart mixer. Water (W) and super-plasticizer (SP) were then added and mixed until a homogeneous cement slurry with controlled rheology was formed. PVA fibers were then slowly added to the wet mixture in the Hobart mixer until a uniform dispersion of fibers was visually evident. The fresh mixture was cast into 152.4 mm × 76.2 mm × 12.7 mm tensile specimens (9 in. × 3 in. × 0.5 in.), covered with plastic sheets, and demolded after 24 hours. The demolded specimens were cured in plastic bags at 95±5% relative humidity (RH) and 20±3 °C for six additional days. After six days, the specimens were removed from the plastic bags and left to cure in ordinary laboratory air regulated at 20 ± 5% RH and 20 ± 3 °C (63-73 °F) for a minimum of 28 days before testing. The final demolded specimens are shown in Figure 2a; specimens with higher carbon content are darker colored, as would be expected. Under optical microscopy and high magnification scanning electron microscopy, the matrix phase appears homogeneously black with no CB agglomeration evident indicating the CB was well dispersed by the mixing method adopted (Figure 3).

Introducing a large volume of porous CB into the ECC system created significant processing challenges with respect to both material workability and the dispersion of PVA fibers. To address this, the amount of water and superplasticizer was adjusted to achieve a homogenous slurry with a plastic viscosity ranging from 7.67 Pa.s (1.11×10^{-3} psi.s) to 10.25 Pa.s (1.49×10^{-3} psi.s) and a yield stress ranging from 5.47 Pa (7.93×10^{-4} psi) to 128 Pa (1.86×10^{-2} psi), as measured by a rotational rheometer. This optimal plastic viscosity range was previously found for ECC without CB to achieve the best PVA fiber dispersion uniformity (Li and Li 2011). To examine the dispersion of the PVA fibers in the CB-ECC specimens, florescence microscopy was adopted to detect and count the number and distribution of PVA fibers in various cross sections of the CB-ECC specimens. The fiber dispersion uniformity was quantified by a fiber dispersion coefficient, α ($0< \alpha \leq 1$ where $\alpha=1$ corresponds to a perfectly uniform fiber dispersion). In the study, α was determined based on an image analysis method applied to the fluorescence images (Li 2009; Lee *et al*. 2009) and was found to be in the range 0.79 to 0.83. However, a reduction in total fiber number at the cross section was found in the CB-ECC specimens as compared to the plain ECC with no CB implying that the high viscosity led to larger pores of entrapped air that in turn reduced the net cross section area (Figure 2b). Thus the introduction of CB into ECC modifies the composite microstructure through rheological changes in the fresh state.

EXPERIMENTAL SETUP FOR ELECTROMECHANICAL CHARACTERIZATION

The CB-ECC stress-strain response was determined under uniaxial tension (Figure 4). The direct uniaxial tensile test is considered to be the most convincing method of evaluating the mechanical attributes of a material; specifically, it reveals if a material exhibits strain hardening behavior. Under flexural loading, some quasi-brittle fiber reinforced cementitious composites can also show "deflection hardening" which is different from strain hardening (Stang 2003). Two linear variable differential transformers (LVDT) were attached to the specimen with gage lengths of 100 mm (3.94 in.) to measure tensile strain during monotonic tensile loading. The load was applied by a standard load frame under displacement control at a constant rate of 0.05 mm/min (1.97×10^{-3} in/min) during the specimen's elastic stage and 0.5 mm/min (1.97×10^{-2} in/min) during its inelastic (*i.e*., strain hardening) stage.

The composite resistivity was measured by the four-point electrical impedance spectroscopy (EIS) method (Figure 4) using a Solartron 1260 impedance analyzer. Compared to 2-point probing with DC signals, the 4-point AC current used during EIS avoids two important characteristics that would affect the measurement of material resistivity: (1) contact impedance which is an interfacial chemical reaction that occurs at the current injection probe, and (2) polarization which is a material dipole effect evident during DC measurements. Both contact impedance and polarization induce time-dependent increases in resistivity. EIS is an electrical testing technique that can be used to characterize the frequency-dependent impedance property of a material. Four electrical contacts (*e.g*., copper tape) were applied onto the surface of each specimen with highly conductive silver colloidal paste. The outer electrodes which pass current into the specimen were spaced 160 mm (6.30 in.) apart. Inner electrodes which measure the *in-situ* voltage within the specimen gage length were spaced 100 mm (3.94 in.) apart. The resistivity measurements were carried out using the impedance analyzer configured for a 100 mV amplitude excitation.

RESULTS: ELECTRICAL PROPERTIES

First, the effect of carbon black content on the bulk resistivity of the prepared specimens was conducted. To measure the resistivity of the specimens, the input AC frequency generated from the impedance analyzer was fixed at 100 Hz because it was found that the resistivity differences between CB-ECC with varied CB content was most prominent in the frequency region 100 to 1000 Hz (Li *et al.* 2011). The bulk resistivities of the 1 year old ECC and CB-ECC specimens are plotted in Figure 5. When CB content increased from 0 to 1% by weight of cementitious ingredients, the material bulk resistivity decreased by an order of magnitude from 1.81×10^{7} Ohm-cm to 1.78×10^{6} Ohm-cm. These results underscore the effectiveness of including nanometer-scale CB as a filler material that is effective in reducing the bulk resistivity of ECC in its unloaded state.

Another set of CB-ECC specimens were fabricated to observe how the bulk resistivity of the material changes with specimen age up to 140 days. Again, a 100 Hz AC frequency was used during measurement of the specimens' resistivity values. The results obtained are plotted in Figure 6. Six specimens were measured for each variation of the CB-ECC material (*e.g*., ECC, CB-ECC 0.25%, CB-ECC 0.5%, and CB-ECC 1.0%). For all of the specimens,

resistivity rapidly increase at an early age (especially up to 28 days) and then plateaus off at approximately 90 days (as evident in Figure 6b). The long-term behavior of specimen resistivity can be explained by the combined effect of the cement hydration process and the pozzolanic reaction (Table 2). The cement hydration process refers to the reaction of tricalcium silicate (C_3S), dicalcium silicate (C_2S), tricalcium aluminate (C_3A) and tetracalcium alumino ferrite (C_4AF) with water (H) to form calcium silicate hydrate (C-S-H), calcium hydroxide and other hydration by-products. This process leads to the loss of water ions and the isolation of pore water, resulting in significant increases in the bulk resistivity of the specimens. The hydration process not only causes a change in the concentration of ions which are the primary charge, but also reduces their mobility by forcing them to take a tortuous path around the C-S-H gel. In addition to cement hydration, the CB-ECC specimens also contain large volumes of fly ash. Fly ash is a pozzolanic material (*i.e.*, a siliceous and aluminous material that reacts with calcium hydroxide in the presence of water). This forms more C-S-H gel in time and further reduces the amount of conductive water ions and retards their mobility. The cement hydration and pozzolanic reactions are summarized in Table 2.

It is interesting to note that the variation in the bulk resistivity measurements of CB-ECC-1.0% is significantly smaller than the other three materials tested, especially compared with the CB-ECC-0 (*i.e.*, regular ECC). This observation substantiates the hypothesis that higher carbon black content reduces the reliance of the electrical conduction mechanism on water ions and hydration products leading to a more stable resistivity measurement. Furthermore, with the addition of porous carbon black, the water absorption capacity of the carbon black results in lower water ionic concentrations. In addition, during the hydration process the water ions are consumed and C-S-H gel is formed. As a result, the resistivity of CB-ECC becomes lower than ECC without CB because the former has a higher amount of conductive carbon.

RESULTS: PIEZORESISTIVE PROPERTIES

Figure 7 shows the mechanical and piezoresistive response of the CB-ECC specimens tested at the age of 28 days. The tensile stress-strain curve contains three stages: (1) elastic response before multiple cracking occurs, (2) strain hardening accompanied by the formation of dense microcrack fields, and (3) tension softening corresponding to localization failure (*e.g.*, fiber pullout) at one of the multiple cracks. While all of the CB-ECC specimens showed strain hardening and multiple cracking behavior, tensile strain capacity varied between the specimens within the range of 0.25 to 1.8%, which is lower than the 2 to 6% of typical ECC (Li and Li 2009). This reduction in strain capacity was due to two reasons: (1) the reduction in average width of the micro-cracks; (2) the reduction of the number of fibers in weak sections of the specimen reducing the fiber bridging capacity. It was found that the average crack width of the CB-ECC specimens was 30-40 μm (during loading) while the average crack width of a standard ECC specimen is 60-70 μm. Single fiber pullout tests reveal a significant enhancement of the fiber-matrix interfacial frictional bond due to the presence of CB particles; this in turn reduced the average crack width. The second cause for the lower strain capacity of the CB-ECC specimens was due to a noticeable reduction in the number of fibers, as revealed by fluorescence microscopy, of the failed (*i.e.,* the weakest) cross section. Reducing the number of fibers had a direct effect on the fiber bridging capacity of the crack leading to early failure under increasing tensile load. It is believed that the reduction in the number of PVA fibers was caused by the increase in plastic viscosity of the fresh material when a large volume of porous CB was incorporated into the matrix. Specifically, the large volume of porous CB introduced larger air pores into the composite thereby reducing the net cross section bridged by the PVA fibers. Regardless, the tensile strain capacity of the CB-ECC specimens was still approximately 25 to 120 times larger than that of concrete or FRCs and one order of magnitude higher than the shrinkage strain of cementitious materials, including ECC-based materials. Drying shrinkage is considered to be the major cause of concrete deck cracking (Saadeghvaziri and Hadidi 2005). The tensile ductility of CB-ECC remains sufficient to suppress early shrinkage cracking (Li and Li 2009). Furthermore, the reduction in average crack width is favorable for resisting chloride penetration through the CB-ECC cover to reach steel reinforcement (Sahmaran *et al.* 2007).

The CB-ECC specimens tested exhibited prominent piezoresistive behavior with resistivity strongly correlated to increased tensile strain. The increase in resistivity is slower during the elastic stage due to the piezoresistivity of the CB-ECC matrix. However, the increase in resistivity accelerates significantly during the inelastic stage due to the formation of microcracks which formed as physical barriers to the conductive path of the ions. Gage factor (i.e., $(\Delta R/R_G)/\varepsilon$ where ΔR is the change in resistivity caused by strain, R_G is the resistivity of the unloaded specimen, and

ε is the applied axial strain) was calculated for the specimens tested. In total three specimens were tested for each version of the CB-ECC composite. The results confirm that increasing the CB content is effective in increasing the CB-ECC gage factor during the elastic regime due to the reduction in the bulk material resistivity. However, a consistent trend in the gage factor is not clear for the inelastic stage. This fact underscores that the formation process of the fields of dense microcracks plays a critical role; since this formation process varies considerable from specimen to specimen, it is difficult to correlate gage factors in the inelastic regime to the material composition. The mechanical and electrical properties for CB-ECC are summarized in Table 3.

To further understand the effect of cracking behavior on the bulk resistivity of the material, 78 images of the cracking pattern of a CB-ECC-1.0% specimen during uniaxial tensile testing was taken at fixed time intervals. Each image was analyzed to count the number of cracks formed at corresponding levels of strain. The relation between crack number, tensile strain and resistivity is plotted in Figure 8. A linear relationship is observed between tensile strain and the number of cracks formed. This suggests an average crack width of 39 μm which corresponds well to observations made using an optical microscope during testing. In contrast, the correlation between resistivity and crack number is non-linear, thereby indicating a non-uniform multiple cracking process (*e.g.*, unequal width of microcracks formed at lower strain versus at higher strain levels; full cracking versus edge cracking; and the spatial networking of cracks). More studies are needed in the future to establish the correlation between resistivity and the cracking pattern in the specimen. Establishment of this correlation would allow the electrical properties of CB-ECC to be used for sensing cracking in structural specimens.

CONCLUSIONS

This study demonstrates the promise of CB-ECC as a multifunctional infrastructure material with damage tolerance and self-sensing capability, both important attributes for materials used in the construction of critical infrastructure systems. By incorporating nanometer-scale CB particles into the ECC system with rheology control, the CB-ECC achieved adequate workability, close-to-uniform PVA fiber dispersion, uniform carbon black dispersion, reduced bulk resistivity, strain hardening behavior with tensile strain capacity of 0.26-1.38%, and reduced crack widths of 30-40 μm during tensile loading. The lower tensile strain capacity of CB-ECC as compared to typical ECC is due to the larger pores of entrapped air that reduce the fiber bridging capacity at the final failure cross section. In addition, the tighter crack widths observed in CB-ECC is due to improvements made in the fiber-matrix interfacial bond. To reduce the number of pores, future work should seek to further optimize the material ingredients, their proportions and rheological properties.

All of the CB-ECC specimens exhibit a prominent piezoresistive behavior with bulk resistivity increasing with tensile strain. A relationship is also observed between the number of cracks formed and bulk resistivity indicating the potential of CB-ECC for future strain and damage sensing. While gage factors have been determined for both the elastic and inelastic stages of CB-ECC tensile behavior, more experimental studies are necessary to establish a more quantitative correlation between resistivity changes and strain as well as between cracking pattern and resistivity. This would lead toward a deeper understanding of the effect of the multiple cracking processes on the variations in gage factors obtained in this study. This includes characterizing the resistivity change under a single crack opening scenario with different stress-crack opening relationships as well as characterizing the resistivity change under various multiple cracking processes caused by the randomness of flaws. Future studies will also focus on: 1) the effect of environmental factors (*e.g.*, temperature, humidity) on the gage factors, 2) understanding the reversal of resistivity changes under cyclic loads; and 3) characterizing residual conductivity changes with residual deformations after unloading.

ACKNOWLEDGEMENTS

The authors gratefully acknowledge the generous support offered by the U.S. Department of Commerce, National Institute of Standards and Technology (NIST) Technology Innovation Program (TIP) under Cooperative Agreement Number 70NANB9H9008.

REFERENCES

Chen, P., and Chung, D. D. L. (1993). "Carbon Fiber Reinforced Concrete as a Smart Material Capable of Non-Destructive Flaw Detection," *Smart Materials and Structures*, Vol. 2, No. 1, pp. 22-30.

Griffith, A. A. (1921). "The phenomena of rupture and flow in solids," *Philosophical Transactions of the Royal Society of London*, A 221, pp. 163–198, http://www.cmse.ed.ac.uk/AdvMat45/Griffith20.pdf .

Hou, T. C., and Lynch, J. P. (2009). "Electrical Impedance Tomographic Methods for Sensing Strain Fields and Crack Damage in Cementitious Structures," *Journal of Intelligent Material Systems and Structures*, Vol. 20, No. 11, pp. 1363-1379.

Kanda, T. and Li, V.C. (1999). "A New Micromechanics Design Theory for Pseudo Strain Hardening Cementitious Composite," *ASCE J. of Engineering Mechanics*, Vol. 125, No. 4, pp. 373-381.

Lee, B. Y., Kim, J. K., Kim, J. S., and Kim, Y. Y. (2009). "Quantitative Evaluation Technique of Polyvinyl Alcohol (PVA) Fiber Dispersion in Engineered Cementitious Composites," *Cement and Concrete Composites*, Vol. 31, No. 6, pp. 408-417.

Li, M. (2009). Multi-Scale Design for Durable Repair of Concrete Structures, Ph.D Thesis, University of Michigan.

Li, M., and Li, V. C. (2009). "Influence of Material Ductility on the Performance of Concrete Repair," *ACI Materials Journal*, Vol. 106, No. 5, pp. 419-428.

Li, M., and Li, V. C. (2011). "Cracking and Healing of Engineered Cementitious Composites under Chloride Environment, " *ACI Materials Journal*, Vol. 108, No. 3, pp. 333-340.

Li, M., Lin, V., Lynch, J., and Li, V. C. (2011). "Multifunctional Carbon Black Engineered Cementitious Composites or the Protection of Critical Infrastructure," RILEM International Conference on High Performance Fiber Reinforced Cement Composites - HPFRCC 6, Ann Arbor, MI, June 20-22, 2011.

Li, V. C. (1993). "From Micromechanics to Structural Engineering--the Design of Cementitous Composites for Civil Engineering Applications." *JSCE J. of Structural engineering and Earthquake Engineering*, Vol. 10, No. 2, pp. 37-48.

Li, V. C. (1998). "Engineered Cementitious Composites – Tailored Composites Through Micromechanical Modeling," *Fiber Reinforced Concrete: Present and the Future*, N. Banthia, A. A. Bentur, and A. Mufti, eds., Canadian Society for Civil Engineering, Montreal, Quebec, Canada, pp. 64-97.

Li, V. C. (2002). "Reflections on the Research and Development of Engineered Cementitious Composites (ECC)," *Proceedings of the JCI International Workshop on Ductile Fiber Reinforced Cementitious Composites (DFRCC) – Application and Evaluation (DRFCC-2002)*, Takayama, Japan, pp. 1-21.

Li, V.C. (2007). "Integrated Structures and Materials Design," *RILEM J. of Materials and Structures*, Vol. 40, No. 4, pp. 387-396.

Li, V. C., Wu, C., Wang, S., Ogawa, A, and Saito, T. (2002). "Interface Tailoring for Strain-Hardening Polyvinyl Alcohol-Engineered Cementitious Composites (PVA-ECC)," *ACI Materials Journal*, Vol. 99, No. 5, pp. 463-472.

Maalej, M., Hashida, T., and Li, V.C. (1995). "Effect of Fiber Volume Fraction on the Off-Crack Plane Energy in Strain-Hardening Engineered Cementitious Composites," *Journal of American Ceramics Society*, Vol. 78, No. 12, pp. 3369-3375.

Marshall, D.B., and Cox, B. N. (1988). "A J-Integral Method for Calculating Steady-State Matrix Cracking Stresses in Composites," *Mechanics of Materials*, Vol. 7, No. 2, pp. 127-133.

Ou, J., and Han, B. (2009). "Piezoresistive Cement-based Sensors and Self-sensing Concrete Components," *Journal of Intelligent Material Systems and Structures*, Vol. 20, No. 3, pp. 329-336.

Peled, A., Torrents, J. M., Mason, T. O., Shah, S. P., Garboczi, E. J. (2001). "Electrical Impedance Spectra to Monitor Damage during Tensile Loading of Cement Composites," *ACI Materials Journal*, Vol. 98, No. 4, pp. 313-349.

Rolander, D. D., Phares, B. M., Graybeal, B. A., Moore, M. E., and Washer, G. A. (2001). "Highway Bridge Inspection: State-of-the-Practice Survey," *Transportation Research Record*, Vol. 1749, No. 1, pp. 73-81.

Saadeghvaziri, M. A., and Hadidi, R. (2005). "Transverse Cracking of Concrete Bridge Decks: Effects of Design Factors," *ASCE Journal of Bridge Engineering*, Vol. 10, No. 5, pp. 511-519.

Sahmaran, M., M. Li, and V.C. Li (2007). "Transport Properties of Engineered Cementitious Composites Under Chloride Exposure," *ACI Material Journal*, Vol. 104, No. 6, pp. 604-611.

Stang, H. (2003). "Scale Effects in FRC and HPRFCC Structural Elements," *High Performance Fiber Reinforced Cementitious Composites*, RILEM Proceedings Pro 30, Eds. Naaman, A.E. and Reinhardt, H.W., pp. 245-258.

Wardhana, K., and Hadipriono, F. C. (2003). "Analysis of Recent Bridge Failures in the United States," *Journal of Performance of Constructed Facilities*, Vol. 17, No. 3, pp. 144-150.

Table 1 – Mix compositions of CB-ECC by weight ratio of cement.

#	*C*	*FA*	*S*	*CB (%)*	*W*	*SP*	*PVA (vol%)*
ECC-I	Type I, 1.0	1.2	0.8	-	0.60	0.01	2.0
CB-ECC-0.25%	Type I, 1.0	1.2	0.8	0.55	0.60	0.013	2.0
CB-ECC-0.5%	Type I, 1.0	1.2	0.8	1.1	0.60	0.016	2.0
CB-ECC-1.0%	Type I, 1.0	1.2	0.8	2.2	0.60	0.022	2.0

Table 2 – Chemical reactions occurring within the CB-ECC material during hydration and curing.

Cement hydration:
$2C_3S + 11H \rightarrow C_3S_3H_8 + 3CH$
$2C_2S + 9H \rightarrow C_3S_3H_8 + CH$
$C_3A + 3C\bar{s}H_2 + 6H \rightarrow C_6A\bar{s}_3H_{32}$
$2C_3A + C_6A\bar{s}_3H_{32} + 4H \rightarrow 3C_4A\bar{s}H_{12}$
$C_4AF + 3C\bar{s}H_2 + 21H \rightarrow C_6(A,F)\bar{s}_3H_{32} + (F,A)H_3$
$C_4AF + C_6(A,F)\bar{s}_3H_{32} + 7H \rightarrow 3C_4(A,F)\bar{s}H_{12} + (F,A)H_3$
Pozzolanic reaction:
$CH + SH \rightarrow CSH$

Table 3 – Mechanical and electrical properties of CB-ECC.

#	*First Cracking Stress (MPa)*	*Cracking Strain*	*Tensile Strength (MPa)*	*Tenile Strain Capacity*	*Strain where Resistivity "Kinks"*	*Resistivity at Kink (kOhm-cm)*	*Initial Resistivity (kOhm-cm)*	*Elastic Gage Factor*	*Inelastic Gage Factor*
CB-ECC-0.25	4.000	0.0895%	4.259	1.375%	0.0643%	129.5 (9.8)	119.7	132.44	198.16
	4.020	0.0716%	4.341	1.050%	0.0518%	75.6 (1.6)	74.0	38.60	163.19
	3.440	0.1452%	4.223	1.280%	0.1336%	116.1 (12.3)	103.8	92.55	176.28
CB-ECC-0.5	3.530	0.0203%[1]	4.000[1]	0.33%[1]	0.0774%[1]	59.1 (0.7)	58.4	9.70[1]	242.75[1]
	3.771 (4.074)	0.0214% (0.0239%)	4.340	0.871%	0.0572%	52.6 (3.3)	49.3	98.46	421.91
	3.954	0.0623%	4.188	1.202%	0.0627%	61.3 (5.3)	56.0	48.4	381.21
CB-ECC-1.0	4.010	0.0703%	4.366	0.631%	0.0513%	113.8 (5.7)	108.2	84.58	279.62
	4.657	0.0247%[2]	5.321	1.008%[2]	0.0471%[2]	105.3 (1.1)	104.2	23.82[2]	202.22[2]
	4.015	0.0221%[1,2]	5.360	0.257%[1,2]	0.0323%[1,2]	97.9 (2.1)	95.8	53.18[1,2]	99.45[1,2]

[1]Severe cracking occurred outside gage length before cracking occurred within gage length.
[2] Final localized failure occurred outside gage length.

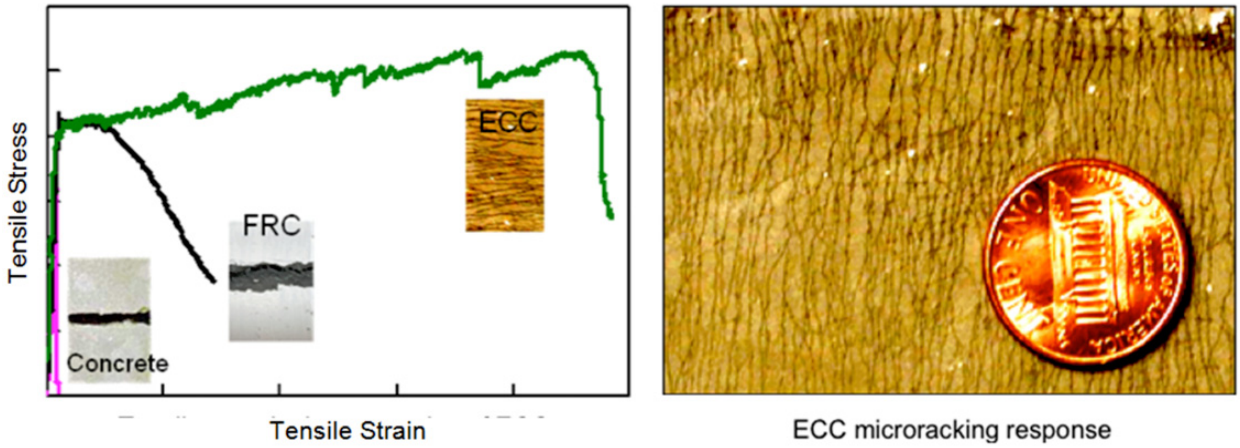

Figure 1 – Engineered Cementitious Composites (ECC): (a) relative stress-strain constitutive properties for ECC compared to traditional concrete and fiber reinforced composites (FRC); (b) field of micro-cracks formed during uniaxial tensile loading.

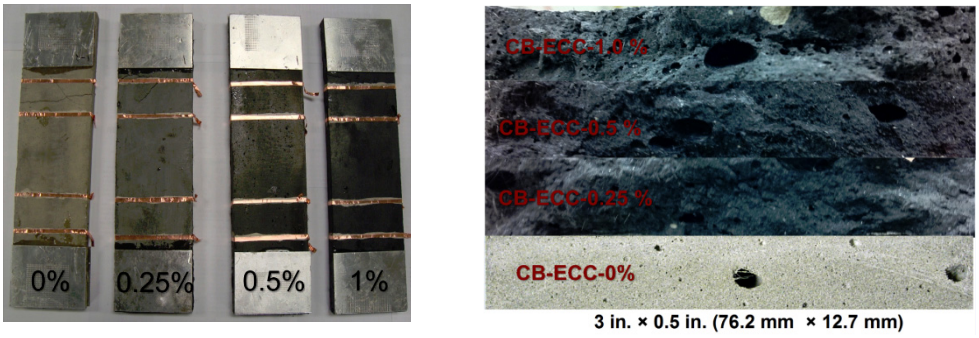

(a) (b)

Figure 2 – (a) CB-ECC specimens with different amounts of carbon black included in the matrix (percentage shown corresponds to the weight percentage of CB to cement plus fly ash weight); (b) corresponding cross section views.

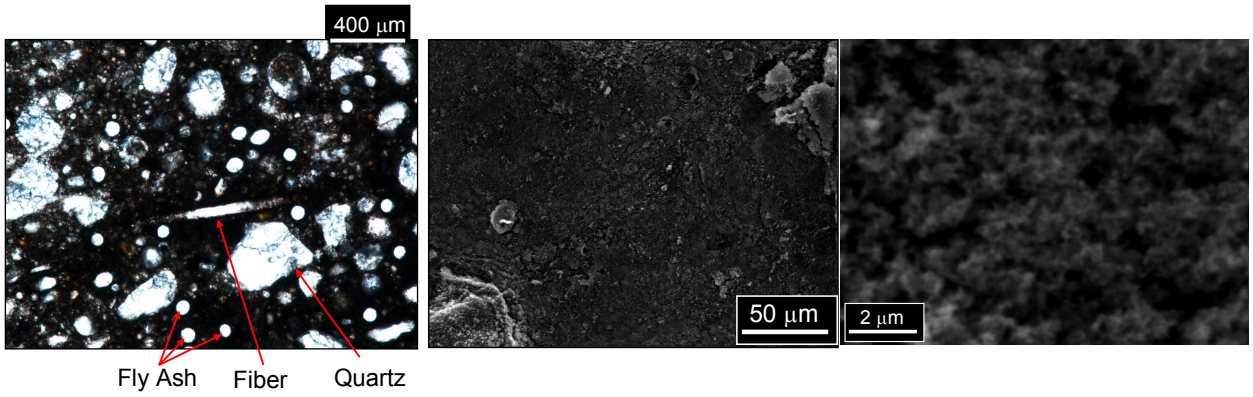

Figure 3 – Characterization of carbon black dispersion in the 0.5% CB-ECC specimen: (left) optical microscopic view; (center and right) scanning electron microscopic views.

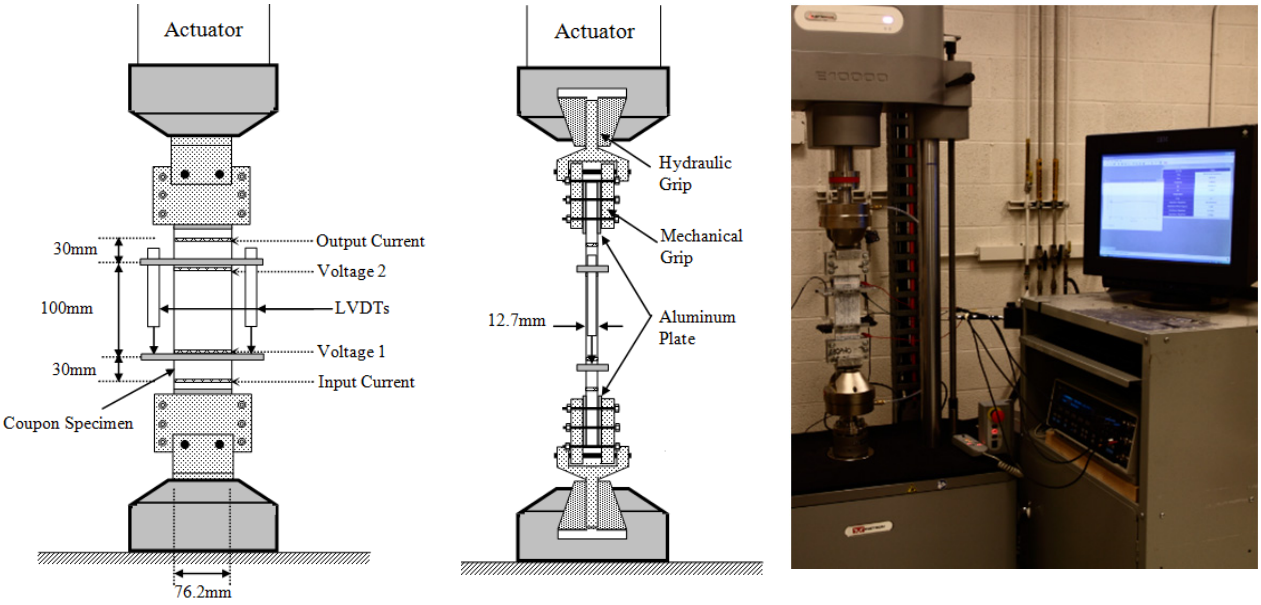

(a) (b) (c)

Figure 4 – Experimental set-up for 4-point electrical impedance spectroscopy of test specimens during uniaxial tensile loading: (a) front view; (b) side view; (c) picture of test set-up with commercial impedance analyzer connected to the CB-ECC specimen.

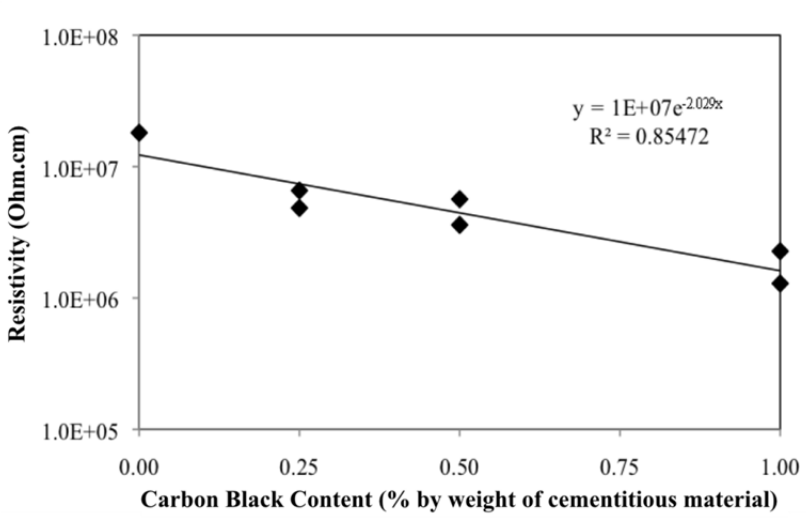

Figure 5 – Bulk resistivity of CB-ECC as a function of the carbon black content (specimen age: 1 year).

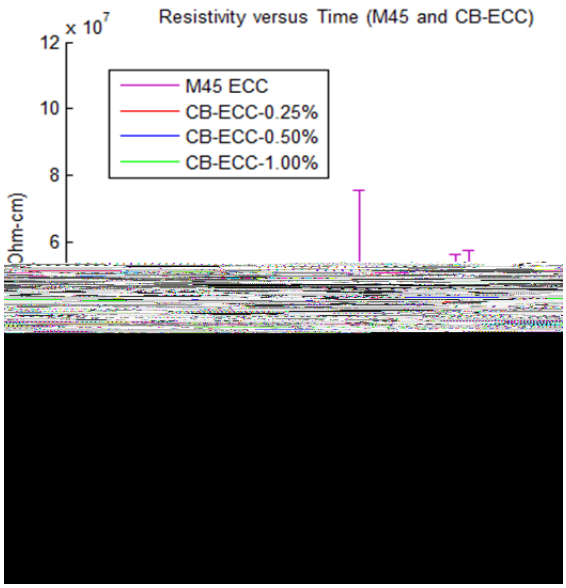

(a) (b)

Figure 6 – Resistivity of CB-ECC specimens versus specimen age with resistivity plotted: (a) linear scale; (b) log-scale.

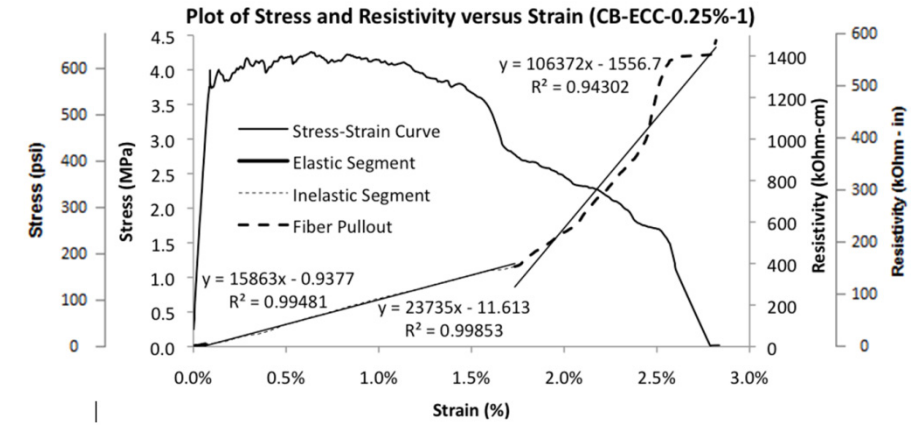

(a)

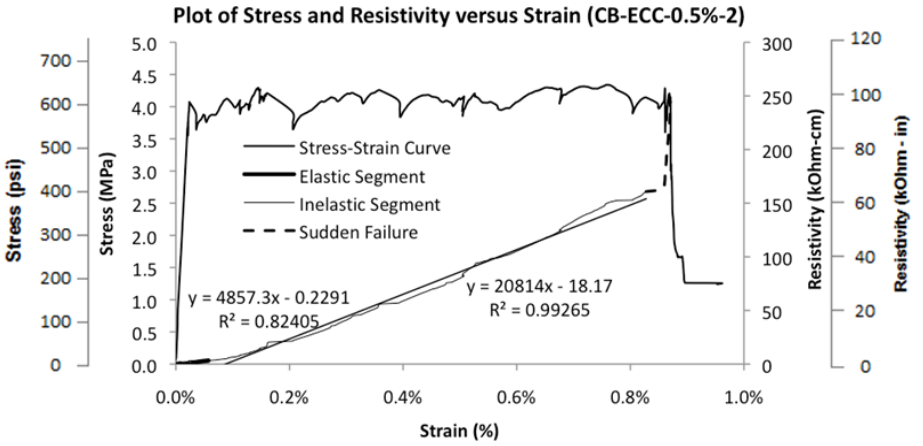

(b)

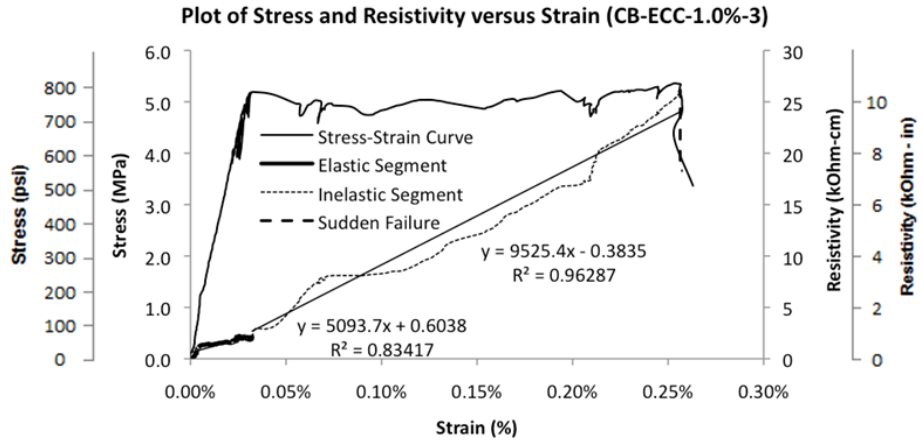

(c)

Figure 7 – Tensile stress-strain curves overlaid with resistivity-strain curves of CB-ECC specimens: (a) CB-ECC 0.25%; (b) CB-ECC 0.5%; (c) CB-ECC 1.0%.

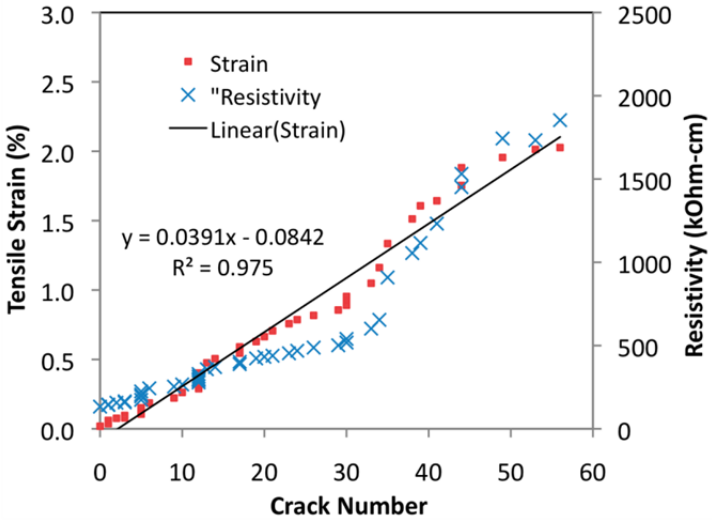

Figure 8 – Correlation between tensile strain, resistivity and crack number of CB-ECC 1.0%.